Research Highlights

- Hydrothermal synthesis of TiO_2-$Ni(SO_4)_{0.3}(OH)_{1.4}$ nanocomposite

- Use of Graphite|TiO_2-$Ni(SO_4)_{0.3}(OH)_{1.4}$ as electrocatalytic anode in alkaline medium

- Electrochemical determination of kinetic parameters for meglumine oxidation

- Facile meglumine electrooxidation revealed by UHPLC-ESI-Q-TOF-MS analysis

- Effective electrooxidation of meglumine also in a commercial formulation

Electrochemical oxidation of meglumine in a pharmaceutical formulation using a nanocomposite anode

G.I. Lozano Gutiérrez[1], O. Ornelas Dávila[1], C. López Aguilar[1], M.M. Dávila Jiménez*[1], R. Silva González[2], I. Sirés[3], E. Brillas[3], D. Fabregat-Safont[4], A.F. Roig Navarro[4], J. Beltrán Arandes[4], J.V. Sancho Llopis[4]

[1] Facultad de Ciencias Químicas, Benemérita Universidad Autónoma de Puebla, Mexico

[2] Instituto de Física, Benemérita Universidad Autónoma de Puebla, Mexico

[3] Laboratori d'Electroquímica dels Materials i del Medi Ambient, Departament de Ciència de Materials i Química Física, Secció de Química Física, Facultat de Química, Universitat de Barcelona, Martí i Franquès 1-11, 08028 Barcelona, Spain

[4] Environmental and Public Health Analytical Chemistry, Research Institute for Pesticides and Water (IUPA), University Jaume I, Avda. Sos Baynat s/n, 12071, Castellón, Spain

*Corresponding author: mdavila.uap.mx@gmail.com (M.M. Dávila Jiménez)

Abstract

The electrocatalytic oxidation of meglumine and gadoterate meglumine (Gd-DOTA) on a TiO_2-$Ni(SO_4)_{0.3}(OH)_{1.4}$ composite anode was investigated in alkaline medium (5 M KOH) using cyclic voltammetry and chronoamperometry. The composite was prepared by hydrothermal method and the morphology and structure of the produced nanoparticles were studied by scanning electron microscopy with energy-dispersive X-ray spectroscopy, X-ray diffraction, atomic force microscopy, BET surface area analysis and Fourier transform infrared spectroscopy. The characterization revealed the formation of $Ni(SO_4)_{0.3}(OH)_{1.4}$ nanobelts dispersed on TiO_2 nanoaggregates. The composite was coated onto a porous graphite rod, showing good adherence without requiring any binder (according to their anodic and cathodic charges). The supported composite was electrocatalytic, allowing the oxidation of meglumine, either as pure reagent or contained in gadoterate meglumine solutions. Electrochemical methods allowed determining the kinetic parameters, such as the electron transfer coefficient α, the total number of electrons n and the standard heterogeneous rate constant k^0 of the reaction of meglumine. The chronoamperometric tests informed about the good stability of the composite anode upon meglumine oxidation at +0.6 V for 10 h. The electrochemical oxidation of meglumine in a commercial pharmaceutical formulation (Dotarem®) was corroborated via ultra-high performance liquid chromatography coupled to electrospray ionization and quadrupole time-of-flight mass spectrometry.

Keywords: Gadoteric acid; Hydrothermal synthesis; Meglumine, Nanocomposite;

Ni hydroxide.

List of symbols and acronyms

ν	Scan rate (mV s^{-1})
Γ	Surface concentration (mol cm^{-2})
$\dot{V}$	Flow rate (cm^3 min^{-1})
AFM	Atomic force microscopy
APIs	Active pharmaceutical ingredients
BET	Brunauer-Emmett-Teller surface area (m^2 g^{-1})
CV	Cyclic voltammetry
E_{an}	Anodic potential (V)
E^0	Standard electrode potential (V)
EDS	Energy-dispersive X-ray spectrometry
E_p	Peak potential (V)
$E_{p/2}$	Half-peak potential (V)
eV	Electronvolt (V)
F	Faraday constant (C mol^{-1})
FTIR	Fourier-transform infrared spectroscopy
Gd	Gadolinium
Gd-DOTA	Gadoterate meglumine
HE	High energy
Hg/HgO	Mercury-mercury oxide reference electrode
HRMS	High resolution mass spectrometry
ICP-MS	Inductively coupled plasma mass spectrometry
I_p	Peak current (mA)
JCPDS	Joint Committee on Power Diffraction Standards card
k^0	Standard heterogeneous rate constant (s^{-1})
LE	Low energy
m/z	Mass-charge
MRI	Magnetic resonance imaging
MS	Mass spectrometry
MS	Multistep mass spectrometry
$[M+H]^+$	Protonated molecule
n	Number of electrons
Pt	Platinum
Q_c	Cathodic charge (in Coulombs)
R	Gas constant (in J mol^{-1} K^{-1})
SEM	Scanning electron microscopy

TOF-MS	Quadrupole time of flight mass spectrometry
t_R	Retention time (min)
UHPLC-ESI-Q-TOF-MS	Ultra high performance liquid chromatography coupled to electrospray ionization and quadrupole time-of-flight mass spectrometry
UPLC	Ultra performance liquid chromatography
XICs	Extracted ion chromatograms
XPS	X-ray photoelectron spectroscopy
XRD	X-ray powder diffraction

1. Introduction

Meglumine is a sugar alcohol derived from glucose that contains an amino group modification. It can be applied either as a counterion to form a salt with active pharmaceutical ingredients (APIs) or as a functional excipient in the pharmaceutical industry and in clinical analysis, since it has low toxicity alongside high biocompatibility and biodegradability [1,2]. Moreover, it can act as catalyst in multicomponent reactions [3,4]. As a counterion, it is typically employed to formulate pharmaceutical contrast agents. Among the contrast agents for magnetic resonance imaging (MRI) examinations, the gadolinium-based MRI contrast agents (GBCAs) are by far the most widely used. A good example is gadoterate meglumine (Gd-DOTA, whose chemical structure is depicted in Fig. 1 [5].

In the commercial pharmaceutical formulation of Gd-DOTA (branded drug DOTAREM®), meglumine is the counterion of (Gd)-1,4,7,10-tetraazacyclododecane-1,4,7,10-tetraacetic acid (DOTA) and favors its solubility. It is often administered to patients for MRI to enhance tissue contrasts.

The use of GBCAs in the last two decades has increased considerably worldwide. Therefore, they are currently considered as emerging contaminants. Once used in clinical studies, GBCAs are excreted mostly unmetabolized, thereby

being discharged into water bodies. Their impact on health and the environment is significant, as they cause anthropogenic Gd abnormalities, which are defined as elevated levels of Gd relative to other naturally abundant lanthanides [6-8]. In this context, several studies and reviews have reported the eco-toxicological impact of GBCAs [9,10], as well as their fate, bioaccumulation, metabolism [11,12], speciation [13,14], stability [15], removal by adsorption [16-19] and degradation of Gd complexes [20].

The recovery and reuse of gadolinium is a growing trend due to its abundant use in clinical analysis and various industrial activities. To address this issue, several strategies have been developed for the removal of rare earth elements and metal ions from aqueous solutions and wastewater [21-23]. However, they are not completely effective for trace levels of contaminants and stable contaminants such like Gd complexes. One of these complexes is the gadoterate meglumine, in which meglumine is the counterion of the macrocycle. Previous studies carried out in our laboratories suggest that meglumine plays an important role in the removal of Gd-DOTA by adsorption or photochemical and electrochemical treatment. In this context, the study of the electrochemical oxidation of meglumine is of interest for a better understanding of Gd recovery.

After clinical analysis, the gadolinium-based compounds are excreted unmetabolized through the urine. Where the two most abundant organic compounds are urea and creatinine [24]. Human urine contains about 0.33 M urea [25], which is a source of energy [26]. When urea is removed from a wastewater stream, it can be used as an energy source when coupled H_2-based fuel cell technologies [26, 27]. Likewise, urine can be efficiently oxidized in an alkaline

medium using nickel oxides or nanostructured materials as electrodes. For this reason, it seems plausible to study them using a nickel-based electrode in alkaline medium. Consequently, considerable efforts have been focused on the synthesis of nanostructures containing nickel oxide, aiming to improve the electrocatalytic property of nickel oxide nanoparticles in alkaline medium [28-31]. So, these nanostructures have received great attention due to their positive catalytic effect in the oxidation of urea   [28,32-34]. On the other hand, basic hydroxy-rich nickel salts have been extensively studied due to their potential applications in areas such as catalysis, anion exchange, sensors and magnetism, among others [35-40]. A basic hydroxy-rich nickel salt is a nickel sulfate hydroxide like $Ni(SO_4)_{0.3}(OH)_{1.4}$. The $Ni(SO_4)_{0.3}(OH)_{1.4}$ catalyst can be synthetized as a nanomaterial by hydrothermal method, according to various reports [41-45]. In addition, in the present work, with the perspective of future studies on the photoelectrochemical degradation of meglumine and gadoterate meglumine in the visible region, TiO_2 was added to $Ni(SO_4)_{0.3}(OH)_{1.4}$ catalyst. On the other hand, nickel and TiO_2 are cheap and very stable catalysts in basic medium. As has been reported, nickel oxides and TiO_2 exhibit high tolerance in alkaline medium, which has favored their use in diverse fields like water treatment and air purification. Authors have revealed their positive characteristics such as chemical stability, insolubility, corrosion resistance, non-toxicity and low cost. [46]. Nickel oxides-TiO_2 composites can be obtained through different methods under different conditions [47-50]. The resulting composite materials are used for energy storage applications, as well as in electrocatalytic and photoelectrocatalytic cells [51,52]. Therefore, they could be used to investigate the redox properties of GBCAs by various electrochemical

techniques. These studies could provide valuable information on the metabolic fate or give rise to new strategies to recover and reuse the gadolinium excreted after clinical analysis. Note that works related to the electrochemical oxidation of GBCAs and its characterization are rather scarce [49,50]. Telgmann et al. [53] reported the potential metabolic pathways of the most frequently used Gd chelates from electrochemistry/capillary electrophoresis/ESI-mass spectrometry (MS) and tandem ICP-MS.

Since gadoterate meglumine is a salt, where meglumine is the counterion, in this first work the electrochemical response and degradation of meglumine are studied. The latter with the aim of knowing if the electrochemical degradation of gadoterate meglumine on a composite electrode could be proposed as the first step to favor the elimination of ionic GBCAs by adsorption, photocatalysis or photoelectrocatalysis. Likewise, in this work, a new hybrid nanomaterial catalyst composed of TiO_2 nanoparticles and $Ni(SO_4)_{0.3}(OH)_{1.4}$ nanobelts was synthesized following a hydrothermal route.

The prepared composite was characterized and its electrocatalytic activity was evaluated by studying the oxidation of both meglumine and gadoterate meglumine in alkaline medium. The electrochemical reactivity of gadoterate meglumine was studied with the future perspective of removing Gd from the Gd-DOTA complex, once excreted in urine, through an electrochemical, photoelectrochemical and adsoption methods. Gadoterate meglumine is a quite stable compound, as verified when treated by different methods. For example, the efficiency of adsorption is reduced due to presence of the meglumine counterion of Gd-DOTA. Therefore, the interest of this work is to evaluate the possible removal

of the meglumine counterion by electrochemical oxidation, which would serve to favor the recovery of Gd-DOTA by adsorption and hence, the recovery of Gd.

2. Experimental

2.1. Materials

TiO$_2$ powder (P25, 99.5%, Degussa, Germany) and meglumine (C$_7$H$_{17}$NO$_5$, Merck) were used without further treatment. NiSO$_4$•7H$_2$O (crystallized, ≥ 99%) and NH$_4$OH (28% NH$_3$ in water, 99.9%) were purchased from Merck. Gadoteric acid was obtained from Dotarem$^®$ (0.5 mmol mL^{-1}) provided by Guerbet. All the solutions were prepared with deionized water.

2.2. Synthesis of basic nickel sulfate nanobelts and the composite

The synthesis of TiO$_2$-Ni(SO$_4$)$_{0.3}$(OH)$_{1.4}$ nanobelts was carried as follows: 0.16 M of NiSO$_4$•7H$_2$O and 0.2 M of NH$_4$OH were dissolved in 15 cm^3 of deionized water under constant stirring at 500 rpm, after which 500 mg of TiO$_2$ P25 powder were added maintaining the stirring. The as-formed green solution was sealed in a Teflon-lined autoclave of 30 cm^3 capacity and maintained at 190 °C for 26 h under stirring. After cooling down to room temperature, the products were collected by naturally sedimentation, washed with distilled water ten times and absolute ethanol twice to remove impurities. The final product was dried at 70 °C overnight. The prepared TiO$_2$-Ni(SO$_4$)$_{0.3}$(OH)$_{1.4}$ composite contained SO$_4^{2-}$ anions intercalated in the nickel hydroxide nanobelts.

2.3. Electrode fabrication

9

For the anode fabrication, 10 mg of the TiO_2-$Ni(SO_4)_{0.3}(OH)_{1.4}$ composite were placed in a tube with 5 cm^3 of ethanol and treated with ultrasounds for 6 min, to disperse the composite material. Then, the nanocomposite was coated onto a porous graphite bar by successive immersion in ethanol solution containing dispersed nanoparticles of the nanocomposite. First, the graphite rod was immersed in a disperse TiO_2-$Ni(SO_4)_{0.3}(OH)_{1.4}$ solution for 6 min and further dried with compressed air. This process was considered as an immersion coating cycle. This procedure was repeated for 20 immersion cycles, without using any binder since the adhesion was very satisfactory, according to their anodic and cathodic charges for the pair Ni(II)/Ni(III) measured before and after each experiment.

2.4. Physical characterization

The crystal structure of the synthesized nickel hydroxyde and nickel-titanium nanomaterials was determined by X-ray powder diffraction (Bruker D8 Discover diffractometer with Cu Kα1 radiation of 1.5401 Å). The morphology and chemical composition of the as-prepared materials were investigated by field emission scanning electron microscope JSM-7800F equipped with an energy-dispersive X-ray spectrometer (EDS). The surface topography of the nickel hydroxide nanobelts was determined by atomic force microscopy (AFM, JEOL JSPM-5200). The textural analysis of the nanocomposite was performed by nitrogen adsorption measured at -196 °C using an Autosorb-1 from Quantachrome. A Nicolet 6700 IR spectrophotometer was used to record in triplicate FTIR transmission spectra with KBr pellets.

2.5. Electrochemical setup

Electrochemical measurements and bulk electrolysis of meglumine solutions were performed in a 20 cm^3 three-electrode undivided cell. The working electrode was a TiO_2-$Ni(SO_4)_{0.3}(OH)_{1.4}$ composite, supported onto porous graphite rod with a geometric area of 4.78 cm^2, and the counter electrode was a Pt mesh. An Hg/HgO (5 M KOH) electrode was employed as the reference electrode, and all the potentials given in this manuscript are referred to it. The electrochemical measurements were made with an Eco Chemie Autolab PGSTAT 302 potentiostat-galvanostat controlled with a GPES 4.9 software. The electrochemical response and stability of the TiO_2-$Ni(SO_4)_{0.3}(OH)_{1.4}$ composite were verified by cycling 10 times from -0.50 to +0.65 V vs. Hg/HgO at a scan rate of 0.003 V s^{-1} in an alkaline medium of 5 M KOH. This high concentration was chosen because the electrocatalytic activity of nickel oxides for the reaction of urea in urine is usually optimal in this medium. It also ensures good stability, durability and corrosion resistance. The response and stability were verified by recording cyclic voltammograms before and after each experiment.

2.6. UHPLC-ESI-Q-TOF-MS analysis

The electrolyzed solutions were adjusted to pH 5.0 and were diluted (1:100) for the analysis of the products by ultra-high-performance liquid chromatography coupled to electrospray ionization and quadrupole time-of-flight mass spectrometry (UHPLC-ESI-Q-TOF-MS). Data were acquired by two acquisition functions at different collision energies (MS^E acquisition mode). The use of the low energy (LE) function with a collision energy of 4 eV provided information about non-fragmented ions related to the parent protonated molecule [M+H]$^+$ in positive ionization mode.

11

The high energy (HE) function, with a collision energy ramp ranging from 15 to 40 eV, allowed the acquisition of accurate-mass fragment ions. A Waters Acquity ultra-performance liquid chromatograph (UPLC) system (Waters, Milford) was employed. The separation was performed using an Atlantis T3 (3.0 mm × 150 mm, 3.0 µm particle size) column from Waters. The mobile phases contained water (A) and methanol (B), both with 0.01% formic acid. The percentage of B changed as follows: 0% at 0 min, 0% at 2 min, 10% at 10 min, 0% at 10.1 min and maintained until 12 min. The flow rate was 800 µL min^{-1} and the analysis run time was 12 min. The sample injection volume was 20 µL.

The UPLC system was interfaced to a hybrid quadrupole-TOF high resolution mass spectrometer (HRMS) (Xevo G2 Q-TOF, Waters Micromass), using an orthogonal Z-spray-ESI interface operating in positive mode. TOF-MS resolution was approximately 18,000 at full width-half maximum at *m/z* 556. Nitrogen was used as drying and nebulizing gas at a flow rate of 1000 dm^3 h^{-1}. The MS data were acquired over an *m/z* range of 50-1000 at a scan time of 0.4 s. A capillary voltage of 0.7 kV and cone voltage of 20 V were used in positive ionization mode. The collision gas was argon (99.995%, Praxair). The desolvation, source and column temperatures were 120 and 40 ºC, respectively.

3. Results and discussion

3.1. Structure and morphology of the synthetized materials

The crystal structure of the synthesized product was determined from comparison of the XRD patterns, shown in Fig. 2. The diffractogram of TiO$_2$

powder, evidencing the anatase and rutile peaks, can be seen in Fig. 2a. The peaks in Fig. 2b can be clearly indexed to a pure monoclinic $Ni(SO_4)_{0.3}(OH)_{1.4}$ (paraotwayite) phase with lattice constants of a = 7.89 Å, b = 2.96 Å, and c = 16.63 Å, according to the standard card JCPDF 41-1424.

Note that no diffraction peaks other than those of nickel sulfate hydroxide can be observed in the XRD pattern of Fig. 2b. Nickel hydroxide nanostructures of various morphologies [54] as well as monoclinic nickel sulfate hydroxide $Ni(SO_4)_{0.3}(OH)_{1.4}$ nanobelts have been obtained under different conditions [41,42,55]. The formation process of the monoclinic nanobelts was proposed by different authors [41-45]. However, the literature on TiO_2-nickel hydroxysulfate composites is scarce [49,50,56]. Fig. 2c illustrates the XRD diffraction pattern of the composite, which maintains the monoclinic phase of the parent nickel sulfate hydroxide.

The morphologies and the surface composition of the nickel sulfate hydroxyde and the as-synthesized TiO_2-$Ni(SO_4)_{0.3}(OH)_{1.4}$ samples were studied by SEM and EDS (Fig. 3 and 4). Fig. 3a and the inset in Fig. 4a reveal that the morphology of nickel sulfate hydroxide consists of nanobelts, whereas that of the TiO_2-$Ni(SO_4)_{0.3}(OH)_{1.4}$ sample presents nanobelts [44] with different lengths dispersed on the TiO_2 aggregates (Fig. 3b and inset of Fig. 4b). In the SEM image shown in Fig. 3b, TiO_2 nanoaggregates, thin nanosheets and nanobelts of different sizes and lengths distributed on the walls and macrocavities of the graphite surface can be identified.

Fig. 4a shows an EDS spectrum of the paraotwayite-type $Ni(SO_4)_{0.3}(OH)_{1.4}$ nanobelts, clearly revealing that the prepared material contains O, Ni and S (note that H is not detectable by EDS). The spectrum confirms the abundance of S, Ni, and O elements (atomic ratio = 1:25:13). In the case of the EDS spectrum of the composite (Fig. 4b), in addition to the elements mentioned above, the presence of Ti in the surface composition stands out. Therefore, the SEM images indicate that the surface is macroporous with a heterogeneos surface distribution of TiO_2-$Ni(SO_4)_{0.3}(OH)_{1.4}$ nanoribbons on TiO_2 nanoaggregates, whereas the sulfate groups are intercalated in the nickel hydroxide, as proven below by FTIR spectroscopy.

The chemical structure of the TiO_2-$Ni(SO_4)_{0.3}(OH)_{1.4}$ composite sample was also identified by FTIR absorption spectroscopy. Fig. S1 shows the FTIR spectrum of both, TiO_2 P25 and the composite, within the wavenumber range between 400 and 4000 cm^{-1}. Different sets of bands can be observed, which correspond to different functional groups. TiO_2 and the composites exhibited strong characteristic peaks of TiO_2. Fig. S1a shows the FTIR spectrum of TiO_2 with a main peak spread from 500 to 700 cm^{-1}, which belongs to Ti-O-Ti bond of the TiO_2 [49], whereas the peak around 1624 cm^{-1} in (a) and (b) in Fig. S1 can be assigned to the bending mode of the physisorbed water on TiO_2 and interlayered water molecules located in the paraotwayite-type layer [56-59]. In Fig. S1b, the vibrational broad bands in the range of 3000 to 3700 cm^{-1} for the composite can be assigned to the O-H stretching vibration of the hydrogen-bound hydroxyl groups and interlayered water molecules located in the paraotwayite-type layer [56-59]. The 1071 and 610 cm^{-1}

bands can be assigned to sulfate groups that are absorbed or coordinated by the surface atoms of $Ni(OH)_2$ layer structure [41,45,57,58]. Gao et al., [45] recently reported via XPS studies that the sulfur element can be incorporated in $Ni(OH)_2$ in the form of sulfate $(Ni(SO_4)_{0.3}(OH)_{1.4})$. The band at 498 cm^{-1} can be assigned to the Ni-O vibrations.

3.2. BET surface area and pore size distribution

The surface area, pore volume and porosity of TiO_2 P25, $Ni(OH)_2$ and TiO_2-$Ni(SO_4)_{0.3}(OH)_{1.4}$ composite samples were investigated by nitrogen adsorption-desorption analysis. Fig. 5a shows the nitrogen adsorption/desorption isotherms of TiO_2 and composite samples, respectively. Isotherms of type IV from Brunauer-Deming-Deming-Teller (BDDT) classification were assigned, suggesting the presence of mesopores (2-50 nm) [60-62]. In composite samples, a high hysteresis loop was observed at a high-pressure range of 0.8-1.0, which can be attributed to interglobular contacts that are generated by the two different components of the material. The isotherms present high absorption within the high relative pressure (P/P_0) range (approaching 1.0), implying the formation of large mesopores. The pore size distribution was calculated from the desorption branch of the nitrogen isotherms by the Barret-Joyner-Halender (BJH) method (not shown). It depicted a peak pore diameter of about 27.5 nm for composite samples, thus confirming the presence of mesopores. The BET surface area of TiO_2 and composite samples was 60 m^2 g^{-1} and the total pore volume was 0.7405 cm^3 g^{-1} for the TiO_2 P25 and 0.4846 cm^3 g^{-1} for the composite sample. The lower total volume of the composite indicates the presence of another component (in this case, nickel hydroxide

sulfate) with lower nitrogen adsorption as compared to titania. Titania nanoparticles were not porous and hence, the same could be expected for the composite. However, the composite showed two substantial differences: smaller adsorbed volume and a hysteresis loop. This is not due to the occurrence of porosity, but to the new cavities formed in the composite due to the nickel phase. Nitrogen adsorption is a convincing method to elucidate such effects.

Aditionally, atomic force microscopy was employed to characterize the topography and the porosity of nickel sulfate hydroxide nanobelts. Fig. 5b and 5c show that the pores can be associated with such nanobelts.

3.3. Electrochemical response of the TiO$_2$-Ni(SO$_4$)$_{0.3}$(OH)$_{1.4}$ nanocomposite

3.3.1. Cyclic voltammetry

The electrochemical oxidation of meglumine was studied in an aqueous basic medium by cyclic voltammetry (CV) using a TiO$_2$-Ni(SO$_4$)$_{0.3}$(OH)$_{1.4}$ nanocomposite supported on a graphite rod electrode. This electrode was previously activated and stabilized by consecutive cyclic voltammetry in 5 M KOH, as described in the section 2.5. Fig. S2a and S2b confirm that the charge associated to the Ni(II)/Ni(III) redox pair after ten activation cycles remained constant. Fig. 6A shows the cyclic voltammetric responses using the TiO$_2$-Ni(SO$_4$)$_{0.3}$(OH)$_{1.4}$ nanocomposite electrode in 5 M KOH (curve *b*) and in the presence of 7.4 mM meglumine (curve *a*) at scan rate of 0.020 V s^{-1}. In the absence of meglumine, the CV data of Fig. 6A(*b*)) highlights the presence of two peaks; the anodic peak appears at 0.485 V and the cathodic one occurs at 0.36 V, which can be assigned to the redox conversion of the Ni(III)/Ni(II) pair described by reaction (1):

16

$$\mathrm{Ni(OH)}_{2(s)} + \mathrm{OH}^{-} \rightleftharpoons \mathrm{NiOOH}_{(s)} + \mathrm{H_2O}_{(l)} + \mathrm{e}^{-} \tag{1}$$
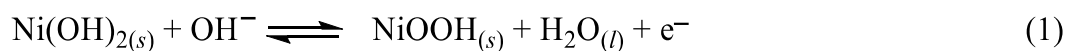
In the presence of meglumine, the anodic peak becomes a wave, and its oxidation occurs in the region of the Ni(II)-to-Ni(III) transition, as can be seen in Fig. 6A(*a*). The contribution of the graphite support to the oxidation of meglumine, shown in the inset (c) of Fig. 6A under the same working conditions, is quite insignificant. After subtracting the background current, the oxidation peak of meglumine is well defined at 0.529 V (see the inset (d) of Fig. 6A). Fig. 6A makes also in evidence that the cathodic peak and the corresponding charge involved in the Ni(III)-to-Ni(II) transition decreases considerably when meglumine is present in the solution, which may suggest the electrocatalytic nature of the oxidation of meglumine. As will be demonstrated later, the degree of disappearance of the cathodic peak depends on the scan rate and the meglumine concentration. It is also very remarkable that during the reverse scan, a broad anodic peak appears at 0.467 V with a high anodic current when meglumine is present in the solution (see arrows in curve *a* of Fig. 6A). The anodic potential during the backward scan (0.467 V) is less positive than that observed during the forward scan (0.529 V). The fact that a high meglumine oxidation current appears at lower anodic potential in the reverse scan suggests the occurrence of desorption of meglumine or intermediates generated during the forward anodic scan.

Fig. 6B shows the cyclic voltammograms obtained with the TiO$_2$-Ni(SO$_4$)$_{0.3}$(OH)$_{1.4}$ composite electrode at different concentrations of meglumine at a scan rate of 0.020 V s^{-1}. As can be seen, the current increases when the meglumine concentration in the solution is risen from 1 mM (curve *a* in inset) to 10

17

mM. For the latter concentration, the anodic peak current increased by approximately 3 times. The insets in Fig. 6B highlight the meglumine oxidation response al low concentration (curve *a*). After removing the background current, the meglumine oxidation peak is about 0.530 V. The electrochemical response by cyclic voltammetry is more noticeable when the forward anodic and backward cathodic scan are represented separately, as shown in Figs. 7A and 7B. As can be observed in Fig. 7A, the onset potential for the Ni(II)/Ni(III) transition during the forward anodic scan is around 0.45 V, and a single oxidation wave is observed at 0.53 V, suggesting that meglumine is indirectly oxidized by Ni(III). Also, Fig. 7B reveals the appearance of an anodic wave in the backward cathodic scan with a less positive potential and with a higher anodic current. The latter indicates that the oxidation continues probably due to the regeneration of Ni(II)/Ni(III) active species because of the removal of intermediates or products resulting from the oxidation of meglumine during the forward scan. This anodic wave in the reverse scan increased upon rise in the concentration of meglumine in the solution. Note that the dependence between the peak current during the backward scan and the meglumine concentration was also linear (inset (b) in Fig. 7B). Linear correlations in Fig. 7A(a) and 7B(b) yield different values for both slopes and intercept. The latter suggests that the intermediates or products resulting from the oxidation of meglumine during the forward anodic scan are also oxidized during the backward cathodic scan. On the other hand, the charge Q_c of NiOOH to $Ni(OH)_2$ decreases with the increase of meglumine in the solution (inset b in Fig. 7B), suggesting that part of the active sites of NiOOH are consumed by meglumine through the indirect

oxidation process. At the same time, the decrease in Q_c is typical of that expected for mediated oxidation described by reactions (1) and (2).

$$\text{NiOOH}_{(s)} + \text{Meglumine} \longrightarrow \text{Ni(OH)}_{2(s)} + \text{products} \tag{2}$$

3.3.2. Effect of the scan rate on meglumine oxidation

The effect of scan rate (v) on meglumine oxidation was evaluated with a 10 mM meglumine and 5 M KOH solution in a range of potential scan rates from 0.003 to 0.2 V s^{-1} (see Fig. 8A). The cyclic voltammograms obtained using the TiO$_2$-Ni(SO$_4$)$_{0.3}$(OH)$_{1.4}$ composite electrode at those rates indicated that the anodic peak current was linearly proportional to the scan rate between 0.003 and 0.2 V s^{-1} (see Fig. 8B), which agrees with a surface-controlled electrode process. From Fig. 8A, one can also establish that the cathodic peak did not shift in potential as the scan rate was increased in the presence of meglumine. However, the cathodic current values observed at low scan speeds increased with rising scan rate, because in short time-scale experiments, there is not enough time for the catalytic reaction to finish. Based on this finding, one can consider that the rate-limiting step is the reaction between Ni oxyhydroxyde and meglumine absorbed on the surface.

The surface concentration (Γ) of meglumine on the surface of TiO$_2$-Ni(SO$_4$)$_{0.3}$(OH)$_{1.4}$ electrode was estimated from the slope of the I_p–v curve, according to the Eq. (3) [63]:

$$I_p = n^2 F^2 A \Gamma v / 4RT \tag{3}$$

where n is the number of electrons transferred (2), F is the Faraday constant (96,485 C mol^{-1}), R is the gas constant (8.314 J mol^{-1} K^{-1}), A is the surface area of

the electrode (4.78 cm^2) and T is the temperature (298 K). From the slope of the anodic peak current vs. scan rate plot, the calculated surface concentration of meglumine was 3.89 x 10^{-9} mol cm^{-2}.

The E_p of the oxidation peak was also dependent on scan rate. The peak potential shifted to more positive values on increasing the scan rate, which confirms the irreversibility of the oxidation process an a linear relationship between peak potential and logarithm of scan rate for CV (Fig. 9A). According to Laviron [64], E_p is defined by the following equation,

$$E_p = E^0 + \left(\frac{2.303RT}{\alpha n_\alpha F}\right) log \left(\frac{RTk^0}{\alpha n_\alpha F}\right) + \left(\frac{2.303RT}{\alpha n_\alpha F}\right) log v \qquad (4)$$

where E^0 is the standard electrode potential, α is the transfer coefficient, k^o is the standard heterogeneous rate constant of the reaction, n is the total number of electrons transferred, v the scan rate, having the other symbols their usual meaning. Thus, the αn-value (i.e., the transfer coefficient for the total step) can be calculated from the slope of E_p vs. log v (slope of 0.0323 V dec^{-1}, Fig. 9A) one can obtain αn = 1.83, from equation (5):

$$m = \frac{2.303RT}{\alpha n_\alpha F} \qquad (5)$$

where α was calculated from the Bard and Faulkner´s [63] equation:

$$\alpha/mV = \frac{47.7}{E_p - E_{p/2}} \qquad (6)$$

where $E_{p/2}$ is the potential at which the current is at half the peak value and hence α = 0.91. Further, the calculated number of electrons (n) transferred in the electrooxidation of meglumine was 2.011 $\approx$ 2. Moreover, from the linear relationship between E_p and v depicted in Fig. 9A, E^0 = 0.5286 V was obtained by

extrapolating the ordinate to $v = 0$. Using this E^0 value, $k^0 = 2.18 \times 10^3$ s^{-1} was calculated by Eq. (7):

$$0.5766 = 0.5286 + \left(\frac{2.303RT}{\alpha n_\alpha F}\right) log \left(\frac{RTk^0}{\alpha n_\alpha F}\right) \tag{7}$$

The dependence of the peak potential and the scan rate-normalized current (I_p $v^{-1/2}$) on the log rate and scan rate, shown in Fig. 9B, demonstrates the characteristic profile of typical electrocatalyst regeneration mechanism [65].

3.3.3. Electrochemical response of gadoterate meglumine

Gadoterate meglumine is a very stable macrocycle (see Fig. 1) and its oxidation, leading to the release of gadolinium, is a challenge. Therefore, the study of its electrochemical behavior is interesting because meglumine acts as a counter ion to form the gadoterate meglumine salt. Fig. 10(A) shows the voltammetric curves with the TiO$_2$-Ni(SO$_4$)$_{0.3}$(OH)$_{1.4}$ electrode in a 5 MM KOH aqueous solution in the presence of 8.8 mM gadoterate meglumine at different scan rates. A single oxidation wave can be observed during the anodic scan, with its peak at around 0.520 V, corresponding to the oxidation of gadoterate meglumine. The current signal in the forward scan is independent of v due to adsorption of gadoterate meglumine on the electrode surface, causing the partial displacement of OH$^-$ ions necessary for the formation NiOOH. In the reverse scan of Fig. 10(A), an anode wave appeared again around 0.497 V with a higher anodic current. This voltammetric behavior is like to that observed with single meglumine, which suggests that the meglumine present in the complex is oxidized during the potential sweep in the anodic direction. This was confirmed by comparing the

voltammetric responses of gadoterate meglumine and meglumine. Fig. 10(B) depicts the voltammogram 9.1 mM meglumine (curve *b*) in 5 M KOH. When 0.1 cm^3 of gadoterate meglumine (8.8 mM) was added to the medium, a considerable increase in current can be observed (curve *c*), and the oxidation potentials during the sweep in the anodic and reverse directions were practically the same. Therefore, it can be considered that only the counterion (meglumine) of the complex is oxidized under our working conditions.

3.3.4. Controlled-potential electrolysis of meglumine

The electrolysis of meglumine was carried out with a TiO$_2$-Ni(SO$_4$)$_{0.3}$(OH)$_{1.4}$ composite electrode in an aqueous solution of 5 M KOH containing 9.1 mM of meglumine at anodic potentials (E_{an}) of +0.460 and +0.6 V under stirring. Fig. 11 shows the change of the oxidation current with time under potentiostatic conditions at E_{an} = +0.6 V. During the first 20 s of electrolysis, the current slowly decreased around 22%; this can be observed from the chronoamperometric curve in inset (a) of Fig. 11. However, after that short time, current increased again until reaching a maximum after 70 min of electrolysis. This behavior may be due to the progressive enrichment of Ni(III) species by oxidation of Ni(II) on the electrode surface at E_{an} = +0.6 V. However, it cannot be ruled out that the catalytic oxidation of meglumine occurs simultaneously during this time. After 70 min of electrolysis, the oxidation current slowly decreases with electrolysis time, almost reaching the initial current, indicating that the composite electrode is very stable and is not deactivated upon prolonged electrolysis. It is pertinent to note that, during the electrolysis of meglumine and gadoterate meglumine, depending on the potential used, the

formation of NiOOH, the oxidation of the compounds/intermediates and the oxygen evolution reaction occur simultaneously. So, the anodic current could be constant depending on the stability of the electrode.

After the electrolysis, the resulting solution was analyzed by UHPLC-ESI-Q-TOF-MS in positive ionization mode to discern if meglumine was completely oxidized. Fig. 12A presents the extracted ion chromatograms (XICs) for (a) blank and for electrolytic trials with 9.1 mM meglumine in solution, (b) before and (c) after 10 h of electrolysis at E_{an} = +0.6 V. According to the chromatogram (Fig. 12A(b)), showing a peak at t_R = 1.04 min, and the corresponding mass spectra (Fig. 12B) obtained at low energy (LE, plot (b)) and high energy (HE, plot (c)), the identified compound is meglumine. The qualifying ions for the identification of meglumine were related to m/z 196, corresponding to the protonated molecule [M+H]$^+$ at LE and with fragment ions m/z of 178, 160 and 129 at HE [3,61,62].

From the determined peak area at t_R = 1.04 min before and after electrolysis, one can conclude that meglumine was degraded by 93%. When the electrolysis of 9.1 mM meglumine was carried out at E_{an} = +0.46 V for 10 h, the oxidation of meglumine was smaller, achieving a 54%.

The electrooxidation of 8.8 mM gadoterate meglumine solution was also performed under the same conditions. Figure S3(a) shows the base peak intensity chromatogram for this solution before electrolysis. The two peaks at t_R = 1.03 and 5.7 min in Fig. S3(a) correspond to meglumine and ^{158}Gd-DOTA components, according to the accurate masses [M+H]. Analysis of the electrolyzed solution by UHPLC-ESI-Q-TOF-MS revealed that the area under the peak at t_R = 1.04 min and

with m/z = 196.1181 (meglumine protonated molecule) decreased by 74% (see Fig. S4A). In contrast, the peak area at t_{R} = 5.71 and m/z = 560.1014 (^{158}Gd-DOTA) practically did not change (see Fig. S5A).

4. Conclusions

XRD, SEM and EDS analyses showed that a hybrid nanoelectrocatalyst composed of TiO_2 nanoparticles and $Ni(SO_4)_{0.3}(OH)_{1.4}$ nanobelts can be synthesized by a hydrothermal method. The prepared TiO_2-$Ni(SO_4)_{0.3}(OH)_{1.4}$ nanocomposite supported on graphite revealed a good electrocatalytic activity for the oxidation of meglumine in an alkaline medium. Cyclic voltammetric analysis with the composite anode in 5 M KOH indicated that the electrochemical oxidation of meglumine occurred through an electrocatalytic-regeneration mechanism. The UHPLC-ESI-Q-TOF-MS analysis of electrolyzed solutions of meglumine and gadoterate meglumine in alkaline medium suggests that meglumine either alone or in the gadoterate is easier to oxidize on a Graphite/TiO_2-$Ni(SO_4)_{0.3}(OH)_{1.4}$ composite electrode than gadoteric acid.

Credit authorship contribution statement

G.I. Lozano Gutiérrez: Investigation. O. Ornelas Dávila: Investigation. C. López Aguilar: Investigation. M.M. Dávila Jiménez: Investigation. R. Silva González: Formal analysis. I. Sirés: Investigation. E. Brillas: Investigation. D. Fabregat-Safont: Formal analysis. A.F. Roig Navarro: Formal analysis. J. Beltrán Arandes: Formal analysis. J.V. Sancho Llopis: Formal analysis.

Declaration of Interest Statement

The authors declare that they have no known competing financial

interests or personal relationships that could have appeared

to influence the work reported in this paper

Acknowledgments

References

[1]   K. Manley, A. Bravo-Nuevo, A.R. Minton, S. Sedano, A. Marcy, M. Reichman, A. Tobia, C.M. Artlett, S.K. Gilmour, L.D. Laury-Kleintop, G.C. Prendergast, Preclinical study of the long-range safety and anti-inflammatory effects of high-dose oral meglumine, J Cell Biochem. 120 (2019) 12051-12062 .https://doi.org/10.1002/jcb.28492.

[2]   T.A. Palchevska, O.O. Saliy, O.P. Baula, K.V. Palchevskyi, O.M. Onishchuk, The role of excipients of trometamolum and meglumine in the formation of biopharmaceutical properties of medicinal products of various pharmacites,

Farmatsevtychnyi Zhurnal 4 (2021) 64-75. https://doi.org/10.32352/0367-3057.4.21.06.

[3] R.Y. Guo, Z. M. An, L.P. Mo, R.Z. Wang, H.X. Liu, S.X. Wang, Z.H. Zhang, Meglumine: A novel and efficient catalyst for one-pot, three-component combinatorial synthesis of functionalized 2-amino-4H-pyrans, ACS Comb. Sci. 15 (2013) 557–563. https://doi.org/10.1021/co400107j.

[4] G. Sravya, G. Suresh, G.V. Zyryanov, A. Balakrishna, K.M.K. Reddy, C. Suresh Reddy, C. Venkataramaiah, W. Rajendra, N. Bakthavatchala-Reddy, A meglumine catalyst–based synthesis, molecular docking, and antioxidant studies of dihydropyrano[3,2-b]chromenedione derivatives, J. Heterocycl. Chem. 57 (2019) 1-15, https://doi.org/10.1002/jhet.3786.

[5] J. Behra-Miellet, G. Briand, M. Kouach, B. Gressier, M. Cazin, J.C. Cazin, On-line HPLC-electrospray ionization mass spectrometry: a pharmacological tool for identifying and studying the stability of Gd^{3+} complexes used as magnetic resonance imaging contrast agents, Biomed. Chromatogr. 12 (1998) 21–26. https://doi.org/10.1002/(SICI)1099-0801(199801/02)12:1%3C21::AID-BMC714%3E3.0.CO;2-Z.

[6] J. Rogowska, E. Olkowska, W. Ratajczyk, L. Wolska, Gadolinium as a new emerging contaminant of aquatic environment, Environ. Toxicol. Chem. 37 (2018) 1523–1534. https://doi.org/10.1002/etc.4116.

[7] R. Brünjes, T. Hofmann, Anthropogenic gadolinium in freshwater and drinking water systems, Water Res. 182 (2020) 115966. https://doi.org/10.1016/j.watres.2020.115966.

[8] P. Ebrahimi, M. Barbieri, Gadolinium as an emerging microcontaminant in water resources: threats and opportunities, Geosci. 9 (2019) 1-44. https://doi.org/10.3390/geosciences9020093.

[9] Y. Fujita, M. Walton, G. Das, A. Dohnalkova, G. Vanzin, A. Anderko, Impacts of anthropogenic gadolinium on the activity of the ammonia oxidizing bacterium Nitrosomonas europaea, Chemosphere 257 (2020) 127250. https://doi.org/10.1016/j.chemosphere.2020.127250.

[10] M. Horstmann, R. Gonzalez de Vega, D.P. Bishop, U. Karst, P.A. Doble, D. Clases, Determination of gadolinium MRI contrast agents in fresh and oceanic waters of Australia employing micro-solid phase extraction, HILIC-ICP-MS and bandpass mass filtering, J. Anal. At. Spectrom. 36 (2021) 767–775. https://doi.org/10.1039/D0JA00493F.

[11] L. Bendakovská, A. Krejčová, T. Černohorský, J. Zelenková, Development of ICP-MS and ICP-OES methods for determination of gadolinium in samples related to hospital wastewater treatment, Chem. Pap. 70 (2016) 1155-1165. https://doi.org/10.1515/chempap-2016-0057.

[12] R.J. McDonald, D. Levine, J. Weinreb, E. Kanal, M.S. Davenport, J.H. Ellis, P.M. Jacobs, R.E. Lenkinski, K.R. Maravilla, M.R. Prince, H.A. Rowley, M.F. Tweedle, H.Y. Kressel, Gadolinium retention: a research roadmap from the 2018 NIH/ACR/RSNA workshop on gadolinium chelates, Radiology 289 (2018) 517–534. https://doi.org/10.1148/radiol.2018181151.

[13] C.L. Kahakachchi, D.A. Moore, Speciation of gadolinium in gadolinium-based magnetic resonance imaging agents by high performance liquid

chromatography inductively coupled plasma optical emission spectrometry, J. Anal. At. Spectrom. 24 (2009) 1389–1396. https://doi.org/10.1039/B907044C.

[14] M. Macke, C.D. Quarles Jr, M. Sperling, U. Karst, Fast and automated monitoring of gadolinium-based contrast agents in surface waters, Water Res. 207 (2021) 117836. https://doi.org/10.1016/j.watres.2021.117836.

[15] M. Birka, J. Roscher, M. Holtkamp, M. Sperling, U. Karst, Investigating the stability of gadolinium based contrast agents towards UV radiation, Water Res. 91 (2016) 244–250. https://doi.org/10.1016/j.watres.2016.01.012.

[16] L. Bendakovská, A. Krejčová, T. Weidlich, Sorption and biosorption of Gd-based contrast agents in the water environment, Chem. Pap. 73 (2019) 2995-3003. https://doi.org/10.1007/s11696-019-00751-8.

[17] M.M. Dávila-Jiménez, M.P. Elizalde-González, M.A. Guerrero-Morales, J. Mattusch, Preparation, characterization, and application of TiO_2/Carbon composite: adsorption, desorption and photocatalysis of Gd-DOTA, Process Saf. Environ. Prot. 120 (2018) 195-205. https://doi.org/10.1016/j.psep.2018.09.012.

[18] M.G. Lawrence, J. Keller, Y. Poussade, Removal of magnetic resonance imaging contrast agents through advanced water treatment plants, Water Sci. Technol. 61 (2010) 685–692. https://doi.org/10.2166/wst.2010.885.

[19] M.P. Elizalde-González, E. García-Díaz, M. González-Perea, J. Mattusch, Removal of gadolinium-based contrast agents: adsorption on activated carbon, Environ. Sci. Pollut. Res. 24 (2017) 8164–8175. https://doi.org/10.1007/s11356-017-8491-x.

[20] M. Cyris, W. Knolle, J. Richard, E. Dopp, C. von Sonntag, T.C. Schmidt, Reaction of Gadolinium chelates with ozone and hydroxyl radicals, Environ. Sci. Technol. 47 (2013) 9942–9949. https://doi.org/10.1021/es402219u.

[21] O. Pereao, L. Petrik, C. Bode-Aluko, O. Fatoba, K. Laatikainen, Rare earth elements removal techniques from water/wastewater: a review, Desalin. Water Treat. 130 (2018) 71–86. http://dx.doi.org/10.5004/dwt.2018.22844.

[22] Ó. Barros, L. Costa, F. Costa, A. Lago, V. Rocha, Z. Vipotnik, B. Silva, T. Tavares, Recovery of rare earth elements from wastewater towards a circular economy, Molecules 24 (2019) 1005-1030. https://doi.org/10.3390/molecules24061005.

[23] I. Wysocka, Determination of rare earth elements concentrations in natural waters–a review of ICP-MS measurement approaches, Talanta (2020) 121636. https://doi.org/10.1016/j.talanta.2020.121636.

[24] K. Carpenter, E.M. Stuve, Electrooxidation of urea and creatinine on nickel foam-based electrocatalysts, J. Appl. Electrochem. 51 (2021) 945–957. https://doi.org/10.1007/s10800-021-01545-1.

[25] H. Marepula, C.E. Courtney, D.G. Randall, Urea recovery from stabilized urine using a novel ethanol evaporation and recrystallization process, Chem. Eng. J. Adv. 8 (2021) 100174. https://doi.org/10.1016/j.ceja.2021.100174.

[26] B.K. Boggs, R.L. King, G.G. Botte, Urea electrolysis: direct hydrogen production from urine, Chem. Commun. (2009) 4859-4861. https://doi.org/10.1039/B905974A.

[27] R. Lan, J.T.S. Irvine, S. Tao, Ammonia and related chemicals as potential indirect hydrogen storage materials, Int. J. Hydrog. Energy 37 (2012) 1482–1494. https://doi.org/10.1016/j.ijhydene.2011.10.004.

[28] X.L. Yang, Y.W. Lv, J. Hu, J.R. Zhao, G.Y. Xu, X.Q. Hao, P. Chen, M.Q. Yan, A three-dimensional nanostructure of NiFe(OH)$_X$ nanoparticles/nickel foam as an efficient electrocatalyst for urea oxidation, RSC Adv. 11 (2021) 17352-17359. https://doi.org/10.1039/D1RA01276B.

[29] D.S. Hall, D.J. Lockwood, C. Bock, B.R. MacDougall, Nickel hydroxides and related materials: a review of their structures, synthesis and properties, Proc. R. Soc. A 471 (2015) 20140792. http://dx.doi.org/10.1098/rspa.2014.0792.

[30] M.T. Bender, Y.C. Lam, S. Hammes-Schiffer, K.S. Choi, Unraveling two pathways for electrochemical alcohol and aldehyde oxidation on NiOOH, J. Am. Chem. Soc. 142 (2020) 21538-21547. https://doi.org/10.1021/jacs.0c10924.

[31] R. Elakkiya, G. Maduraiveeran, Three-dimensional nickel−cobalt oxide nanomaterials as enzymemimics electrocatalyst for the glucose and lactic acid oxidation reaction, New J. Chem. 43 (2019) 14756-14762. https://doi.org/10.1039/C9NJ01291E.

[32] F. Guo, K. Ye, K. Cheng, G. Wang, D. Cao, Preparation of nickel nanowire arrays electrode for urea electrooxidation in alkaline medium, J. Power Sources 278 (2015) 562-568. https://doi.org/10.1016/j.jpowsour.2014.12.125.

[33] R.M. Abdel-Hameed, R.H. Tammam, Nickel oxide nanoparticles grown on mesoporous carbon as an efficient electrocatalyst for urea electro-oxidation,

Int. J. Hydrogen Energy 43 (2018) 20591-20606. https://doi.org/10.1016/j.ijhydene.2018.09.088.

[34] W. Yan, D. Wang, L.A. Diaz, G.G. Botte, Nickel nanowires as effective catalysts for urea electro-oxidation, Electrochim. Acta 134 (2014) 266-271. https://doi.org/10.1016/j.electacta.2014.03.134.

[35] M. Meyn, K. Beneke, G. Lagaly, Anion-exchange reactions of hydroxy double salts. Inorg. Chem. 32 (1993) 1209-1215. https://doi.org/10.1021/ic00059a030.

[36] K.J. Kim, J.E. Ellis, B.H. Howard, P.R. Ohodnicki, Centimeter-scale pillared-layer metal–organic framework thin films mediated by hydroxy double salt intermediates for CO_2 sensor applications, ACS Appl. Mater. Interfaces 13 (2021) 2062-2071. https://doi.org/10.1021/acsami.0c19621.

[37] E. Coronado, J.R. Galán-Mascarós, C. Martí-Gastaldo, A. Ribera, E. Palacios, M. Castro, R. Burriel, Spontaneous magnetization in Ni-Al and Ni-Fe layered double hydroxides, Inorg. Chem. 47 (2008) 9103-9110. https://doi.org/10.1021/ic801123v.

[38] Z. Zhang, Y. Zhao, Z. Zhao, G. Huang, Y. Mei, Atomic layer deposition-derived nanomaterials: oxides, transition metal dichalcogenides, and metal–organic frameworks, Chem. Mater. 32 (2020) 9056-9077. https://doi.org/10.1021/acs.chemmater.9b04414.

[39] C. Duan, L. Dong, F. Li, Y. Xie, B. Huang, K. Wang, Y. Yu, H. Xi, Room-temperature rapid synthesis of two-dimensional metalorganic framework nanosheets with tunable hierarchical porosity for enhanced adsorption

desulfurization performance, Ind. Eng. Chem. Res. 59 (2020) 18857-18864. https://doi.org/10.1021/acs.iecr.0c02437.

[40] J. Liu, Z. Wang, K. Su, D. Xv, D. Zhao, J. Li, H. Tong, D. Qian, C. Yang, Z. Lu, Self-supported hierarchical IrO_2@NiO nanoflake arrays as an efficient and durable catalyst for electrochemical oxygen evolution, ACS Appl. Mater. Interfaces 11 (2019) 25854–25862. https://doi.org/10.1021/acsami.9b05785.

[41] Z.Y. Jia, From layered $Ni(OH)_2$ thin films to $Ni(SO_4)_{0.3}(OH)_{1.4}$ nanobelts through SO_4^{2-} inserting in colloid-based route, Adv. Mater. Res. 295-297 (2011) 1548-1553. https://doi.org/10.4028/www.scientific.net/AMR.295-297.1548.

[42] L. Li, J. Liang, M. Luo, J. Fang, Highly qualified fabrication of $Ni(SO_4)_{0.3}(OH)_{1.4}$ nanobelts via a facile TEA-assisted hydrothermal route, Powder Technol. 226 (2012) 143-146. https://doi.org/10.1016/j.powtec.2012.04.033.

[43] T. Gao, B.P. Jelle, Paraotwayite-type α-$Ni(OH)_2$ nanowires: structural, optical, and electrochemical properties, J. Phys. Chem. C 117 (2013) 17294-17302. https://doi.org/10.1021/jp405149d.

[44] Y. Tang, Z. Jia, Y. Jiang, L. Li, J. Wang, Simple template-free solution route for the synthesis of $Ni(SO_4)_{0.3}(OH)_{1.4}$ nanobelts and their thermal degradation, Nanotechnology 17 (2006) 5686-8690. https://doi.org/10.1088/0957-4484/17/22/025.

[45] M. Gao, L. He, Z.Y. Guo, Y.R. Yuan, W.W. Li, Sulfate-functionalized nickel hydroxide nanobelts for sustained oxygen evolution, ACS Appl. Mater. Interfaces 12 (2020) 443-450. https://doi.org/10.1021/acsami.9b14216.

[46] J, Yang, J. Du, X. Li, Y. Liu, C. Jiang, W. Qi, K. Zhang, C. Gong, R. Li, M. Luo, H. Peng, Highly hydrophilic TiO_2 nanotubes network by alkaline hydrothermal method for photocatalysis degradation of methyl orange, Nanomaterials 9 (2019) 526, https://doi.org/10.3390/nano9040526

[47] J. Yu, Y. Hai, B. Cheng, Enhanced photocatalytic H_2-production activity of TiO_2 by $Ni(OH)_2$ cluster modification, J. Phys. Chem. C 115 (2011) 4953–4958. https://doi.org/10.1021/jp111562d.

[48] S. Kumar-Lakhera, B. Neppolian, Role of molecular oxygen on the synthesis of $Ni(OH)_2/TiO_2$ photocatalysts and its effect on solar hydrogen production activity, Int. J. Hydrogen Energy 45 (2020) 7627-740. https://doi.org/10.1016/j.ijhydene.2019.10.142.

[49] A. Meng, S. Wu, B. Cheng, J. Yu, J. Xu, Hierarchical $TiO_2/Ni(OH)_2$ composite fiber with enhanced photocatalytic CO_2 reduction performance, J. Mater. Chem. A 6 (2018) 4729-4736. https://doi.org/10.1039/C7TA10073F.

[50] M.J. Gómez, R.O. Lucci, E.A. Franceschini, G.I. Lacconi, Effect of TiO_2 content on Ni/TiO_2 composites electrodeposited on SS316L for hydrogen evolution reaction, Electrochim. Acta 378 (2021) 138136. https://doi.org/10.1016/j.electacta.2021.138136.

[51] M. Botta, M. Ravera, A. Barge, M. Bottaro, D. Osella, Relationship between ligand structure and electrochemical and relaxometric properties of acyclic

poly(aminocarboxylate) complexes of Eu(II), Dalton Trans. (2003) 1628-1633. https://doi.org/10.1039/B211533F.

[52] M. Gál, F. Kielar, R. Sokolová, Š. Ramešová, V. Kolivoška, Electrochemical study of the EuIII/EuII redox properties of complexes with potential MRI ligands, Eur. J. Inorg. Chem. 18 (2013) 3217–3223. https://doi.org/10.1002/ejic.201300252.

[53] L. Telgmann, H. Faber, S. Jahn, D. Melles, H. Simon, M. Sperling, U. Karst, Identification and quantification of potential metabolites of Gd-based contrast agents by electrochemistry/separations/mass spectrometry, J. Chromatogr. A 1240 (2012) 147–155. https://doi.org/10.1016/j.chroma.2012.03.088.

[54] L. Dong, Y. Chu, W. Sun, Controllable synthesis of nickel hydroxide and porous nickel oxide nanostructures with different morphologies, Chem. Eur. J. 14 (2008) 5064–5072. https://doi.org/10.1002/chem.200701627.

[55] J.S. Chen, S.P. Huang, D.J. Blackwood, Composition-dependent pseudocapacitive properties of self-supported nickel-based nanobelts, J. Phys. Chem. C 121 (2017) 7101–7107. https://doi.org/10.1021/acs.jpcc.7b00452.

[56] Q. Jiang, Y. Qiu, K. Yan, J. Xiao, S. Yang, Self-assembly of Ni_2P nanowires as high-efficiency electrocatalyst for dye-sensitized solar cells, MRS Commun. 2 (2012) 97–99. https://doi.org/10.1557/mrc.2012.16.

[57] D. Yang, P. Liu, Y. Gao, H. Wu, Y. Cao, Q. Xiao, H. Li, Synthesis, characterization, and electrochemical performances of core-shell $Ni(SO_4)_{0.3}(OH)_{1.4}$/C and NiO/C nanobelts, J. Mater. Chem. 22 (2012) 7224–7231. https://doi.org/10.1039/C2JM30237C.

[58] S. Zhang, H.C. Zeng, Self-assembled hollow spheres of β-Ni(OH)$_2$ and their derived nanomaterials, Chem. Mater. 21 (2009) 871–883, https://doi.org/10.1021/cm8028593.

[59] M. Ocaña, Preparation and characterization of uniform needle-like particles of nickel basic sulfate, J. Colloid Interface Sci. 228 (2000) 259–262. https://doi.org/10.1006/jcis.2000.6950.

[60] M. Thommes, K. Kaneko, A.V. Neimark, J.P. Olivier, F. Rodriguez-Reinoso, J. Rouquerol, K.S.W. Sing, Physisorption of gases, with special reference to the evaluation of surface area and pore size distribution (IUPAC Technical Report), Pure Appl. Chem. 87 (2015) 1051-1069. https://doi.org/10.1515/pac-2014-1117.

[61] K.S.W. Sing, D.H. Everett, R.A.W. Haul, L. Moscou, R.A. Pierotti, J. Rouquerol, T. Siemieniewska, Reporting physisorption data for gas/solid systems — with special reference to the determination of surface area and porosity, Pure Appl. Chem. 54 (1982) 2201-2218. https://doi.org/10.1351/pac198254112201.

[62] J. Yu, J. Zhang, A simple template-free approach to TiO$_2$ hollow spheres with enhanced photocatalytic activity, Dalton Trans. 39 (2010) 5860-5867. https://doi.org/10.1039/C0DT00053A.

[63] A.J. Bard, L.R. Faulkner, Electrochemical methods, Fundamentals and applications, John Wiley & Sons, New York, 2001.

[64] E. Laviron, General expression of the linear potential sweep voltammogram in the case of diffusionless electrochemical systems, J. Electroanal. Chem.

Interfacial Electrochem. 101 (1979) 19–28. https://doi.org/10.1016/S0022-0728(79)80075-3.

[65] V. Vedharathinam, C.G. Botte, Understanding the electro-catalytic oxidation mechanism of urea on nickel electrodes in alkaline medium, Electrochim. Acta 81 (2012) 292–300. https://doi.org/10.1016/j.electacta.2012.07.007.
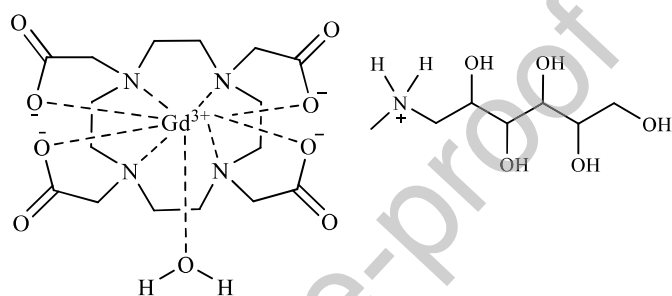
Fig. 1. Structural formula of gadoteric acid (i.e., Gd-DOTA) in solution.
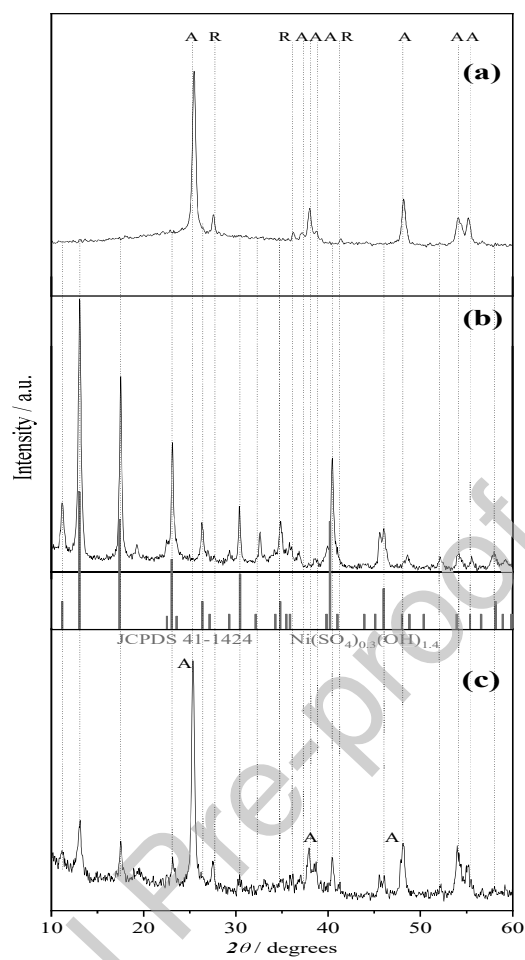
Fig. 2. XRD patterns of (a) TiO_2 P25, (b) $Ni(SO_4)_{0.3}(OH)_{1.4}$ and (c) composite.
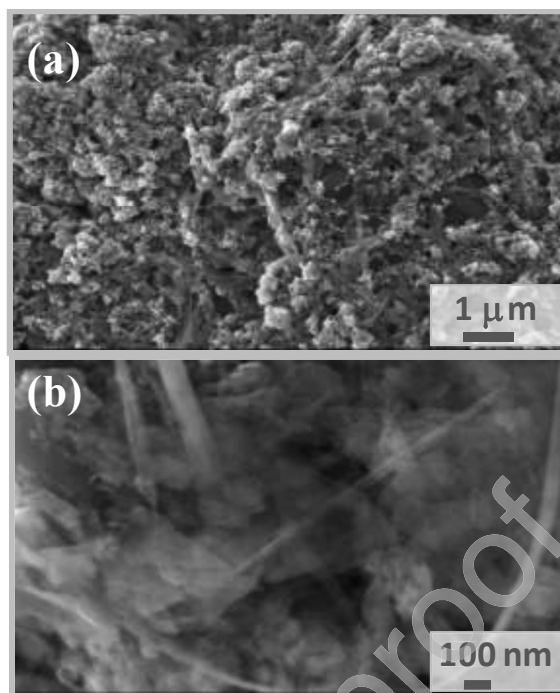
Fig. 3. SEM images of the (a) $Ni(SO_4)_{0.3}(OH)_{1.4}$ nanobelts and (b) TiO_2-$Ni(SO_4)_{0.3}(OH)_{1.4}$ composite.
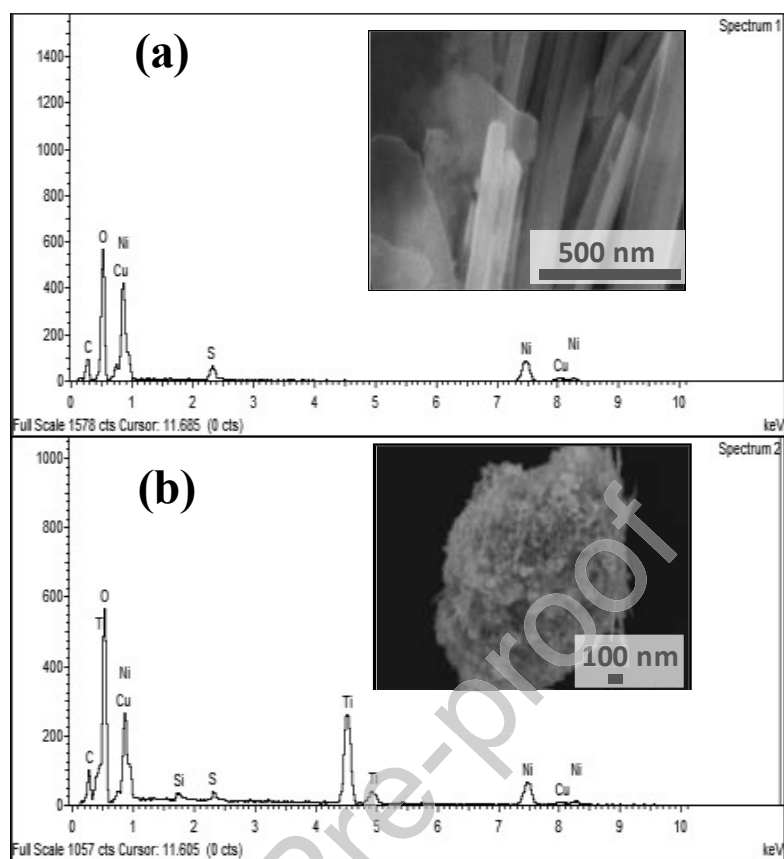
Fig. 4. EDS pattern of (a) the as-synthesized paraotwayite-type $Ni(SO_4)_{0.3}(OH)_{1.4}$ nanobelts and (b) the TiO_2-$Ni(SO_4)_{0.3}(OH)_{1.4}$ composite.
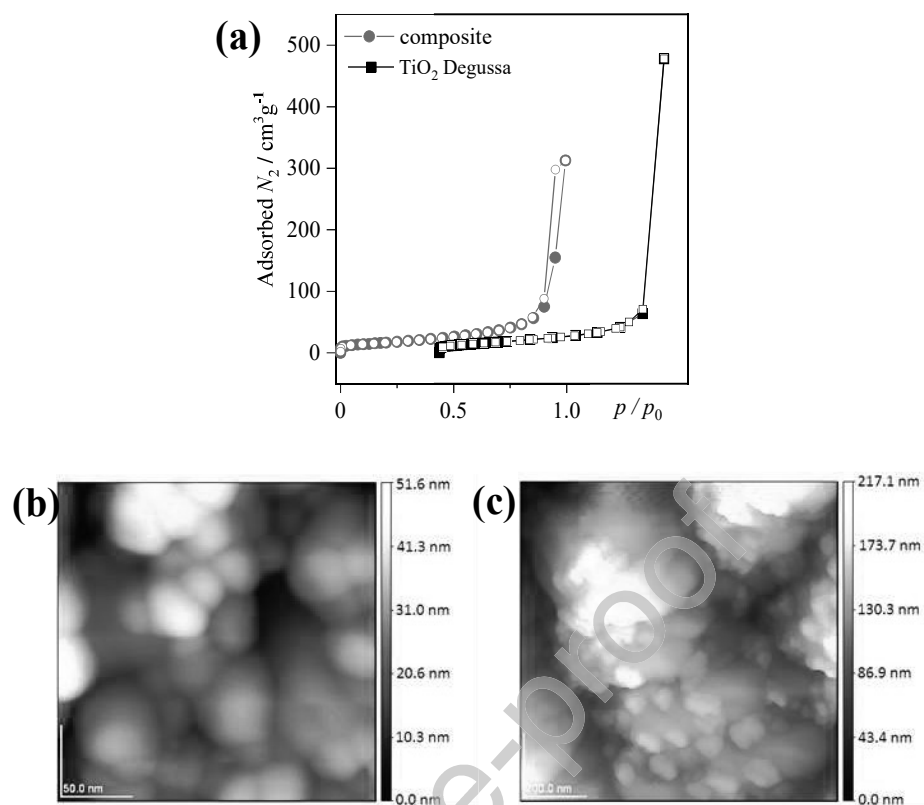
Fig. 5. (a) Nitrogen adsorption-desorption isotherms of the composite and of TiO_2 shifted 0.5 p/p_0 units for clarity. (b,c) AFM images of nickel sulfate hydroxide nanobelts.
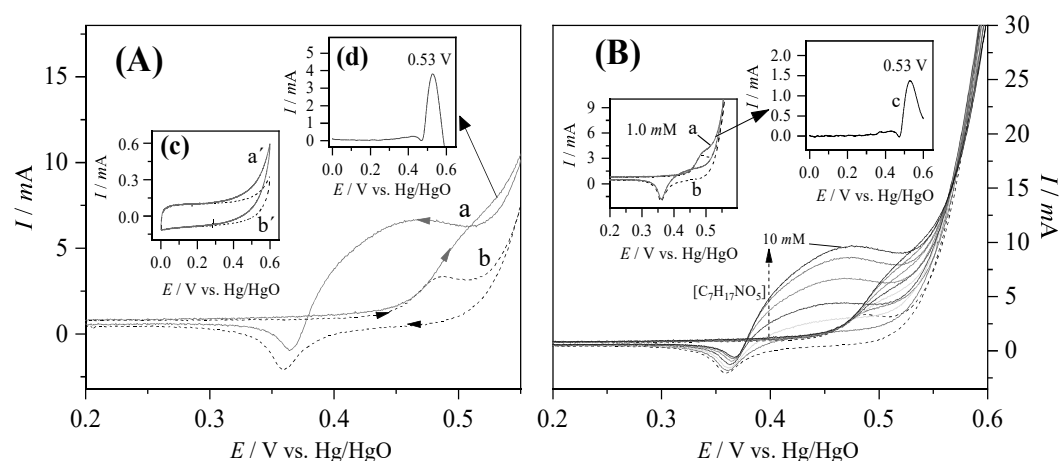
Fig. 6. (A) Cyclic voltammograms obtained with TiO_2-$Ni(SO_4)_{0.3}(OH)_{1.4}$ nanocomposite in 5 M KOH solution (curve *b*) and in the presence of 7.4 mM meglumine (curve *a*). Inset (c), voltammograms on graphite without (curve *b'*) and with (*a'*) 7.4 mM meglumine. Inset (d), voltammogram after subtracting background current. (B) Cyclic voltammograms with the TiO_2-$Ni(SO_4)_{0.3}(OH)_{1.4}$ nanocomposite in 5 M KOH solution (dashed curve) and in the presence of different concentrations of meglumine: 1, 2, 4.8, 7.4 , 9.1 and 10 mM. Insets in Fig. 6B show the voltammograms of 1 mM meglumine before (curve *a*) and after (curve *c*) subtracting background current. Scan rate of 0.020 V s^{-1}.

41
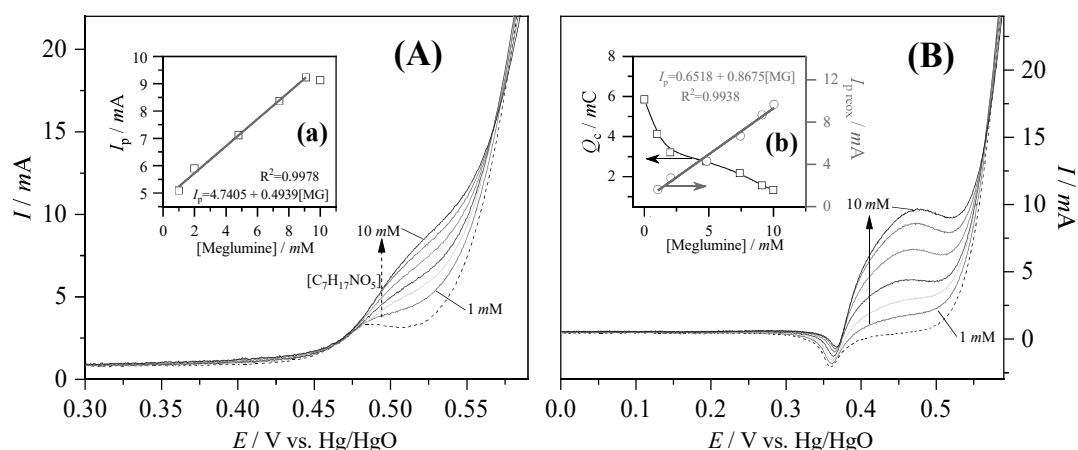
Fig. 7. Potentiodynamic curves at different concentrations of meglumine in solution during potential sweep in (A) the anodic direction and (B) the cathodic direction. Meglumine concentrations are the same as in Fig. 6. Dependence of the intensity of the anodic peak current at 0.52 V with the concentration of meglumine (inset (a) in A). Variation of the cathodic charge and the cathodic peak current with the concentration of meglumine in the solution (inset (b) in B). Scan rate 0.020 V s^{-1}.
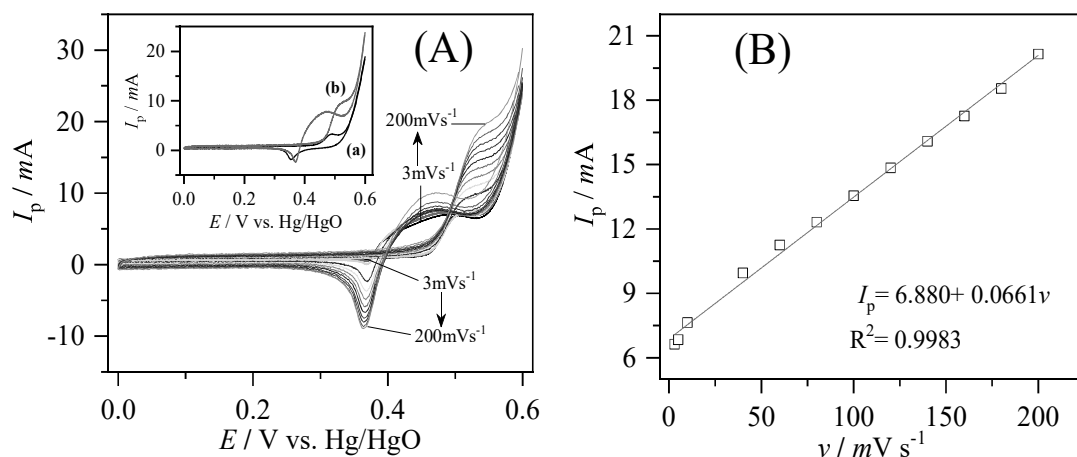
Fig. 8. (A) Cyclic voltammograms at different scan rates (from 0.003 to 0.20 V s^{-1}) using the TiO$_2$-Ni(OH)$_2$ composite electrode, recorded in 10 mM meglumine with 5 M KOH solution. Inset in (A), voltammograms of 5 M KOH solution (curve a) and in the presence of 10 mM meglumine (curve b). (B) Plot of I_p versus v for cyclic voltammograms depicted in (A).
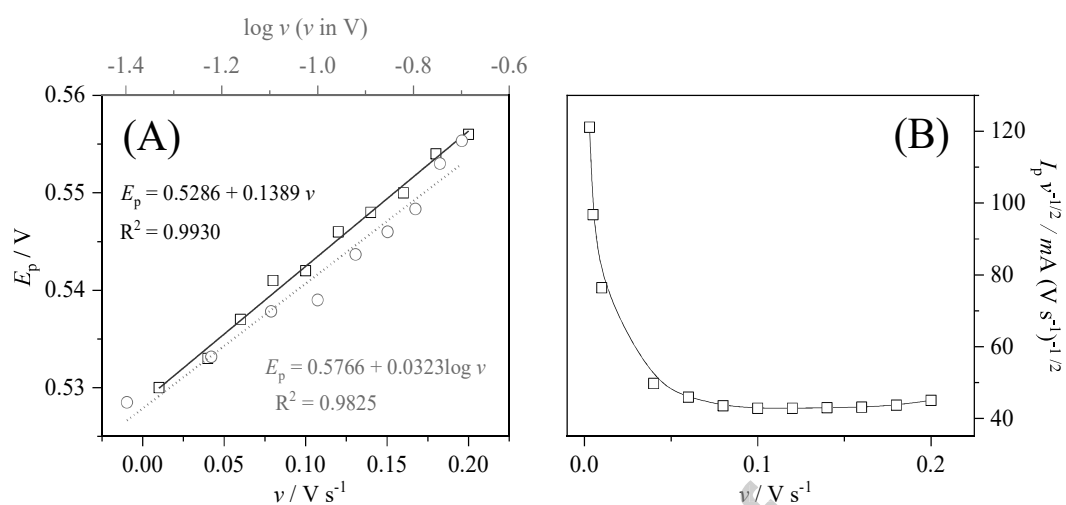
Fig. 9. (A) Plot of anodic peak potential (E_p) with scan rate (v from 0.010 to 0.20 V s^{-1}) and E_p with log v (v from 0.040 to 0.20 V s^{-1}). (B) Relationship between I_p $v^{-1/2}$ and scan rate (v from 0.003 to 0.20 V s^{-1}).
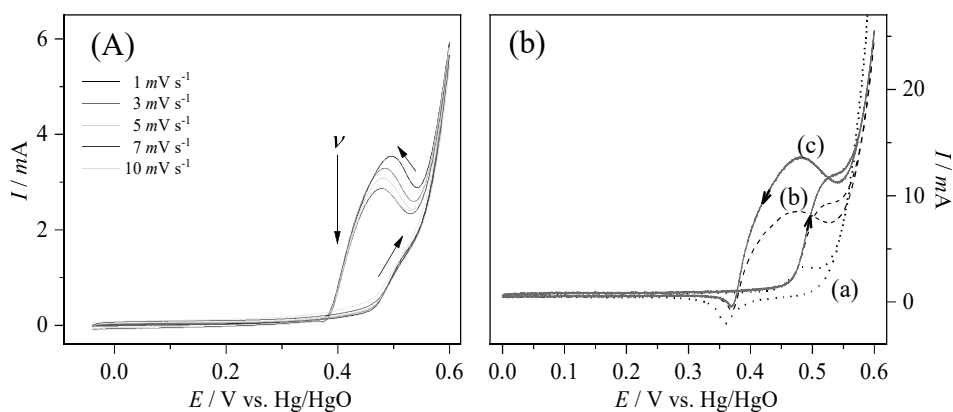
Fig. 10. (A) Voltammetric response of 8.8 mM gadoterate meglumine in 5 M KOH solution using the TiO_2-$Ni(SO_4)_{0.3}(OH)_{1.4}$ composite electrode at low scan rates. (B) Effect of the addition of 8.8 mM Dotarem[®] (curve *c*) to the reaction medium containing 9.1 mM meglumine (curve *b*), considering the voltammetric response in 5 M KOH (curve *a*) at scan rate of 0.020 V s^{-1}.
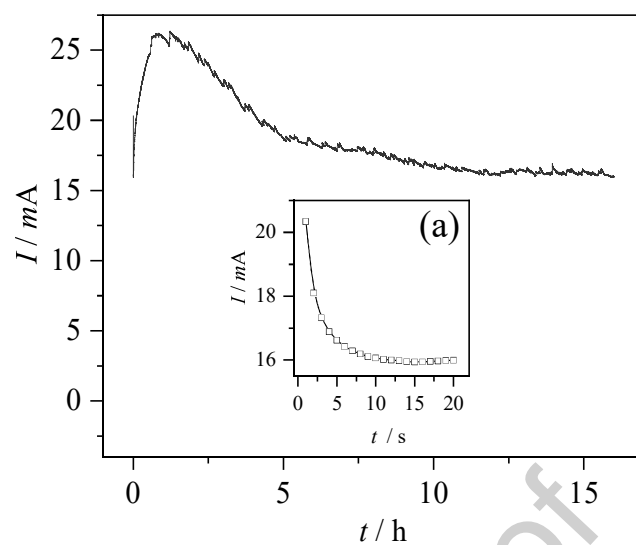
Fig. 11. Chronoamperogram obtained using the TiO_2-$Ni(SO_4)_{0.3}(OH)_{1.4}$ composite electrode in the presence of 9.1 mM meglumine in 5 M KOH at an anodic potential value (E_{an}) of +0.6 V. Inset (a), chronoamperometric curve of meglumine oxidation.
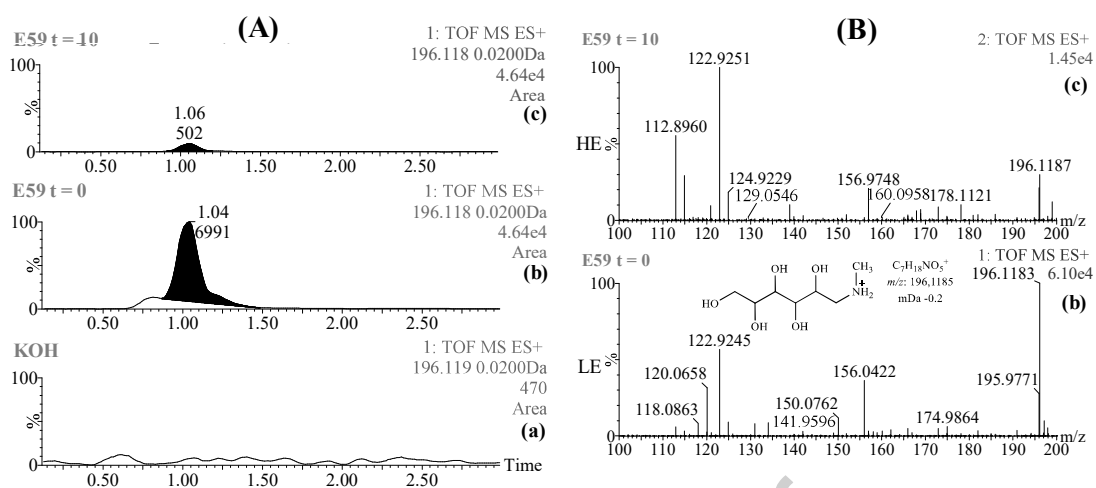
46

Fig. 12. (A) LE extracted ion chromatograms (XIC) for solutions: (a) 5 M KOH, (b) 9.1 mM meglumine in 5 M KOH before electrolysis and (c) after electrolysis at E_{an} = +0.6 V and t = 10 h. (B) In plot (b), mass spectra in LE of 9.1 mM meglumine; in plot (c) mass spectra at high energy (HE) before electrolysis. The pH of the solutions was adjusted to 5.0.